Article type: Full Paper

The role of oxygen doping on elemental intermixing at the PVD-CdS/Cu(InGa)Se_2 heterojunction

Xiaoqing He, Peter Ercius, Joel Varley, Jeff Bailey, Geordie Zapalac, Tim Nagle, Dmitry Poplavskyy, Neil Mackie, Atiye Bayman, Vincenzo Lordi, Angus Rockett**

Dr. X. He, Prof. A. Rockett
Materials Science and Engineering, University of Illinois at Urbana-Champaign,
1304 W. Green Street, Urbana, Illinois 61801, USA
E-mail: arockett@illinois.edu
Dr. P. Ercius
Lawrence Berkeley National Laboratory National Center for Electron Microscopy,
Cyclotron Road Mail Stop 72-150, Berkeley, CA 94720, USA
Dr. J. Varley and Dr. V. Lordi
Materials Science Division, Lawrence Livermore National Laboratory,
7000 East Avenue, Livermore, CA 94550, USA
E-mail: lordi2@llnl.gov
Dr. J. Bailey, Dr. G. Zapalac, Dr. T. Nagle, Dr. D. Poplavskyy, Dr. N. Mackie, Dr. A. Bayman
MiaSolé Hi-Tech,
2590 Walsh Ave, Santa Clara, CA 95051, USA

Keywords: Cu(In,Ga)Se_2 photovoltaics, CdS Structure, Cu diffusion, scanning transmission electron microscopy, STEM-EDS mapping

Elemental intermixing at the CdS/$CuIn_{1-x}Ga_xSe_2$ (CIGS) heterojunction in thin-film photovoltaic devices plays a crucial role in carrier separation and thus device efficiency. Using scanning transmission electron microcopy in combination with energy dispersive X-ray mapping, we find that by controlling the oxygen in the sputtering gas during physical vapor deposition (PVD) of the CdS, we can tailor the degree of elemental intermixing. More oxygen suppresses Cu migration from the CIGS into the CdS, while facilitating Zn doping in the CdS from the ZnO transparent contact. Very high oxygen levels induce nanocrystallinity in the CdS, while moderate or no oxygen content can promote complete CdS epitaxy on the CIGS grains. Regions of cubic Cu_2S phase were observed in the Cu-rich CdCuS when no oxygen is included in the CdS deposition process. In the process-of-record sample (moderate O_2) that exhibits the

highest solar conversion efficiency, we observe an ~26 nm thick Cu deficient CIGS surface counter-doped with the highest Cd concentration among all of the samples. Cd movement into the CIGS was found to be less than 10 nm deep for samples with either high or zero O_2. The results are consistent with the expectation that Cd doping of the CIGS surface enhances device performance.

1. Introduction

$CuIn_{1-x}Ga_xSe_2$ (CIGS)-based thin film solar cells continue to show promise in the renewable energy market due to a steady gain in their solar energy conversion efficiencies in commercial scale devices.[1-5] The choice for the buffer layer in CIGS cells to form a p-n heterojunction for carrier collection is usually CdS, which typically yields the highest performing devices. The CdS is often deposited by a "wet" chemical bath deposition (CBD) method, although alternative methods for forming CdS and other Cd-free buffer layers have been explored.[6-9] For compatibility with an in-line vacuum production line, "dry" physical vapor deposition (PVD) of CdS may be preferred and can be implemented without vacuum breaks in a full-stack deposition tool. However, early PVD-CdS/CIGS devices exhibited inferior efficiency compared to their CBD-CdS/CIGS counterparts.[10] This difference cannot be explained solely by poor coverage of the PVD-CdS buffer layer on the CIGS surface as previously thought.[10, 11] One possible explanation was suggested by D. Abou-Ras *et al*.[11] that the lack of a buried p-n homojunction at the PVD-CdS/CIGS interface could be responsible. Subsequently, a PVD-CdS/CIGS solar cell with 14.5% efficiency was demonstrated at lab scale.[12] The authors concluded that post-annealing of the PVD-CdS/CIGS device was an essential step to achieve this high efficiency, conjecturing that chemical interdiffusion across the interface formed a buried p-n homojunction in the CIGS subsurface related to Cd occupying Cu depletion sites at the CIGS surface, similar to what occurs during the CBD CdS process. This suggests that further optimization of the PVD-CdS/CIGS fabrication process can improve the solar cell efficiency. A PVD-CdS/CIGS flexible solar module with an aperture area of 7583 cm^2 from MiaSolé demonstrated a 16.3% efficiency under global AM1.5 solar illumination (999.3 W/m^2) (measured by Fraunhofer ISE)[13]. We recently reported the microstructural and chemical nature of the PVD-CdS/CIGS heterojunction in the Miasolé production line device and found large epitaxial CdS domains of both zinc-blende phase and wurtzite phase grown on the CIGS

surface, which are not usually formed during the CBD CdS process.[14] This could have significant implications for the possibility of collection of photo-generated carriers from the buffer layer, which until now has not been observed, improving electron transport through the buffer to the transparent contact, as well as potentially reducing interface recombination. Furthermore, we also showed the presence of Cu rich domains in the CdS and the concurrent Cd doping layers on the CIGS surface, suggesting the formation of a *p-n* homojunction at the CdS/CIGS interface[15, 16].

Absorbed light loss in the CdS window layer is a known limiting factor for further improving the quantum efficiency in the blue light region. An oxygenated CdS thin film deposited via reactive sputtering was proven to be effective in increasing the bandgap of the window layer and thus benefiting the performance of CdS/CdTe solar cells[17, 18]. So far, no comprehensive investigation at atomic scale has been presented of the effects of the concentration of oxygen on the structure of the oxygenated thin films and the resulting CdS/CIGS solar cell devices.

In this paper, we investigate systematically, three different PVD-CdS/CIGS heterojunctions fabricated on the Miasolé production line using advanced scanning transmission electron microscopy (STEM) combined with energy dispersive X-ray spectroscopy (EDS). The major difference among the samples is the oxygen content employed in the sputtering gas during PVD-CdS deposition. Table I shows the measured performance parameters of each device, and corresponding quantum efficiency data for devices processed under identical conditions is given in **Figure 1**. SBR64(ZERO) (no O_2) exhibits good performance. With increasing O_2 addition the device performance gradually improves as seen in SBR64(LOW) and SBR64(POR) before decreasing at the highest levels. SBR64(MAX) with the highest O_2 delivers the lowest efficiency, mostly as a result of bias-dependent collection. This implies that modest incorporation of O in the CdS process is beneficial for maximizing the device performance. This is reminiscent of the observation in $CdCl_2$ treatment of CdTe/CdS junctions, where addition of O_2 is known to improve the resulting devices.[19, 20] Therefore, it is very

interesting to study the underlying microstructural and chemical differences associated with addition of O_2 to the process gas among the four samples.

We found that very high O content results in nanocrystalline CdS and suppresses Cu migration from the CIGS into the CdS, while enhancing Zn doping in CdS from the ZnO transparent contact overlayer. In the sample without O, Cu sometimes was found distributed through the entire CdS layer. Interestingly, pure Cu_2S phase was observed in the $Cd_xCu_{1-x}S$ matrix as well. Among all of the samples, SBR64(POR), with modest O content, shows the best epitaxy and crystallinity of CdS. In addition, Cu depletion and Cd counter-doping are found below the CIGS surface, but in SBR64(POR) the Cd doping is most significant with the highest doping concentration and the largest doping depth (see text below and Figures S1, S2, and S3), implying the possible formation of a more deeply buried p-n junction in the CIGS near interface region. This suggests that high quality CdS epilayers on the CIGS surface and the formation of a more deeply buried p-n homojunction related to the Cu depletion and Cd doping on CIGS surface may be beneficial for raising the conversion efficiency of CIGS/CdS solar cells.

2. Experimental Section

Samples studied here were all fabricated in MiaSolé's production equipment using process settings similar to the standard manufacturing settings. All layers in the devices are deposited sequentially onto flexible stainless steel substrates in a single pass all-PVD process system with no vacuum break.

All of the transmission electron microscopy (TEM) samples were prepared by a lift-out method on a FEI Helios Nanolab 600i focused ion beam (FIB) instrument. To reduce the Ga ion surface damage and implantation, a small current and voltage (8 *p*A, 1kV) were used for the final polishing step. To protect the fresh samples from being oxidized gradually in air, the samples were stored in a special TEM sample preservation capsule that could be evacuated and back filled with dry nitrogen. Immediately before analysis, all of the TEM samples were cleaned

using a Fischione Model 1040 NanoMill specimen preparation system to further minimize the Ga-induced amorphous layer and damage. STEM-EDS maps were acquired in a FEI Titan TEM operating at 200kV at the National Center for Electron Microscopy, Molecular Foundry, Lawrence Berkeley National Lab. The EDS detector is a Super-X quad windowless detector with a collection solid angle of 0.7 steradian enabling elemental mapping typically in several minutes. The K lines of all elements were utilized for EDS maps and quantification. Before acquiring EDS maps, the heterojunctions were oriented to a CIGS [021] zone axis where clear high resolution TEM images of the hetero-interface could be recorded without any indication of overlap between the CIGS grains and CdS layers to ensure that the interface was parallel to the electron beam. After acquiring the EDS maps, the area of interest was carefully examined in HREM image mode to make sure that EDS maps came from exactly where the HREM images were recorded.

3. Results and discussion

3.1 CdS No Oxygen Sample

A typical STEM-EDS map from sample SBR64(ZERO) is shown in Figure 2, where the most notable feature is the deeply depleted Cd region in the CdS (dark region in Figure 2a, denoted by a circle) filled by a high concentration of Cu (Figure 2b). Figure 2d shows that no significant Zn doping of the CdS from the ZnO is observed, which is different from some other samples with O in the CdS, as discussed below. Quantitative EDS analysis reveals the composition of the circled area in Figure 2a to be Cu 66.0±6.6%, Cd 0.6±0.6%, and S 33.4±3.8% (all compositions here and below are given in at. %), which is very close to Cu_2S, although we are unable to distinguish this composition from other phases such as $Cu_{1.9}S$ without improved calibration standards. [The error values associated with the compositions here are based on the standard deviation in the data (i.e. precision of the data). Averages of all data points typically yielded atomic percentages reliable to three significant figures (i.e. accuracy of

the data). Therefore we list tree significant figures on compositions despite high scatter in some measurements.] A high resolution TEM (HRTEM) image recorded in this Cu_2S region, which is processed using an HREM image filtering plug-in[21] in Digitalmicrograph^{TM} to reduce the noise, is shown in Figure 3.The hetero-interface is coherent with clear lattice fringes present on both sides of the interface. The yellow square in Figure 3 corresponds to the circled region in Figure 2a. The fast Fourier transform (FFT) taken from the square region, shown in the inset, reveals the structure, which is described well by cubic Cu_2S with lattice parameters consistent with the Cu_2S powder diffraction file card number 00-053-0522 (5.56 Å). Thus, we conclude that the heterojunction partner material in some portions of the heterojunction is Cu_2S, epitaxially grown on the CIGS with the same orientation relationship that we previously reported for cubic CdS on CIGS.[14] Cu_2S is a known semiconductor with a band gap of about 1.2 eV[22]. It is typically *p*-type. Cu_2S was widely studied in 1960s-80s in the context of Cu_2S/CdS solar cells.[23, 24] With a comparable band gap to CIGS, Cu_2S can potentially form its own collecting heterojunction with the CdS surrounding it.

In addition, there is appreciable Cd content observed up to ~7.5 nm into the CIGS (Figure 2a, also see Figure S1). For example, the composition of the CIGS within the rectangle in Figure 2a was determined to be Cu 22.2±2.2%, Cd 2.4±0.8%, In 15.8±2.7%, Ga 9.5±1% and Se 50.1±4.7%, which indicates a Cu deficient CIGS surface layer doped by Cd. The Cd doped layer penetrates quite far into the CIGS and should result in *n*-type material there, leading to the formation of a buried p-n homojunction in the CIGS, similar to what has been proposed in CBD-CdS by many authors.[25-27] Ramanathan *et al.*[28] suggested, for example, that Cd doping of the CIGS surface holds the key to the success of CBD-CdS buffer layers. The same behavior appears to hold for this PVD-CdS.

The presence of Cu_2S at the heterojunction has several effects detectable from analysis of the current/voltage and quantum efficiency results from this device. First, there is an order of magnitude increase in J_0 for this device (see Table I), resulting in a lower open circuit voltage,

V_{oc}. This may result from either increased interface recombination or higher defect density in the CIGS. It could also result from reduced inversion of the heterojunction or a change in the heterojunction band offsets that would make carrier collection unfavorable. However, we observe significant Cd doping of the CIGS so reduced inversion appears unlikely. Second, there is significant current loss in the blue portion of the spectrum for this device as can be seen in the QE data. Furthermore there is an apparent decrease in the effective energy gap of the "CdS" layer by ~0.2 eV, as would be expected with the introduction of Cu into the CdS and the absence of O in the buffer material.

Simulation of the device using the SCAPS device simulation program[29] shows the best fit based on a change in heterojunction band offsets resulting from the combination of a lower CdS energy gap in the absence of O incorporation and a dipole at the heterojunction that further increased the electron affinity. The experimental data, in particular low Voc, was found to be most consistent with a negative (cliff-like) band offset in the conduction band.

Our recent theoretical calculations show that the Cd vacancies (V_{Cd}^{-2}) are the most energetically stable native defect in *n*-type CdS and are attracted electrostatically to copper interstitials (Cu_i^{+}), which can cause the formation of Cu_{Cd}^{-} acceptor defects.[30, 31] The EDS maps show a fading intensity of Cu along with an increasing intensity of Cd toward the ZnO side of the CdS, which suggests that Cd ions and Cu ions may go through a cation exchange process.[32] Apparently there is a strong driving force for exchange of Cd and Cu to such an extent that in some areas the two change places completely, resulting in replacement of CdS with Cu_2S and distribution of the missing Cd well into the CIGS. We note that there are several quaternary CuCd(In,Ga)Se compounds described in the literature[33], supporting the idea that mixing of Cd into the CIGS is favorable. However, we did not observe evidence of such specific phases here in either the EDS compositional analyses or the TEM images. Finally, we note that the amount of Cu observed in the CdS greatly exceeds the amount of Cu missing from the region of the CIGS studied by EDS in the TEM. Analysis of the sample deeper into the

CIGS showed that Cu depletion extends well beyond the region of Cd doping, more than 40 nm into the sample.

3.2 CdS High Oxygen Sample

Stoichiometric CdS has a direct band gap of about 2.4 eV, which causes the absorption of light at wavelengths below ~550 nm and reduces the quantum efficiency in the blue region of the solar spectrum. Wu *et al.* reported that incorporation of O into CdS by a sputtering process can increase the band gap and reduce the crystallinity of CdS.[34] That paper also reported a much improved J_{sc} of CdTe/Cd(O,S) solar cells while maintaining high V_{oc} and fill factor. Kephart *et al.* also demonstrated a National Renewable Energy Laboratory verified 15.2% efficiency CdS/CdTe cell on 3.2-mm soda-lime glass by optimizing the deposition of a sputtered, oxygenated thin CdS window layer on CdTe absorber.[17] However, sample SBR64(MAX) studied here with the highest O content shows the lowest efficiency among our four samples (see Table I), demonstrating that too much O is detrimental.

Figure 4 shows typical EDS maps from SBR64(MAX). No resolvable Cu is found in the CdS in this sample (Figure 4b), suggesting that high concentrations of O_2 in the sputtering gas can prevent Cu from migrating into the CdS. This phenomenon is similar to the report by Wu *et al.*[34] that oxygenated CdS can inhibit Te diffusion from CdTe into CdS. A closer examination reveals that there is a Cu depletion layer at the CIGS surface (denoted by two dashed red lines in Figure 4b, also see Figure S2) and filled by some Cd (Figure 4a). This indicates that this sample also includes a Cu deficient CIGS surface doped by Cd ions. Because no Cu was found in the CdS, these observations suggest that the surface was Cu deficient before the deposition of CdS. Liao *et al.* [25, 26] previously showed the presence of a Cu depleted CIGS surface, which could facilitate Cd doping. It was proposed that this was due to the surface reconstruction of the cation-terminated (112) polar surface,[25, 35] which has a low energy in CIGS. It was noted that the absence of Cu would reduce the electric dipole energy before CdS

deposition, as supported by density functional theory calculations by S.-B. Zhang *et al.*[35] However, the Cu depleted CIGS surface layer is about 10 nm thick in our study (see Figure S2). EDS quantification from the white rectangle in Figure 4a gives a composition of Cu 21.2±2.1%, Cd 3.5±1.2%, Ga 12.6±1.4%, In 9.6±2.1%, Se 43.6±4.2%, O 9.5±1.5%. This composition is significantly anion rich, probably as a result of the presence of O at relatively high levels. We did not detect any obvious oxide phases accompanying the oxygen incorporation into the CIGS. The Cd doping concentration is slightly higher than SBR64 (ZERO), and the Cd doping depth is about 10 nm, as measured from the composition line profile (see Figure S2). The incorporation of O into the CIGS could be related to the diffusion of sputtering gas containing O_2 and Ar from the CdS deposition zone into the CIGS deposition zone rather than to post-preparation oxidation. The TEM samples were well preserved in a dedicated TEM sample capsule that had been evacuated and backfilled with dry N_2. Furthermore, no oxygen was found in other similarly-handled samples that would have been expected to show similar behaviors if the TEM samples were oxidizing prior to analysis.

An additional striking difference of sample SBR64(MAX) relative to other samples is that Zn and O are distributed throughout the CdS layer, despite the fact that the CdS deposition occurred before the ZnO deposition. Therefore, something about the nanochemistry and nanostructure of the CdS when deposited with high levels of oxygen promoted movement of Zn into the CdS layer during ZnO deposition. HRTEM images (Figure 5) taken from the same location as the EDS maps (Figure 4) show that the (Cd,Zn)(O,S) buffer layer is nanocrystalline. We expect that further increases of O incorporation into the CdS would completely amorphize the structure.[34]

Several dramatic changes are observed in the device performance as a result of the process conditions used for SBR64(MAX). The device exhibits a similar dark current/voltage behavior as for the other devices (Table I) with a moderately increased reverse saturation current, J_0, and ideality factor, a, relative to the process-of-record device. However, the series resistance

increased by a factor of 10. The major change is the behavior under light, where strong voltage-dependent collection results in a large loss of fill factor. Analysis of the QE data shows that the energy gap of the heterojunction partner materials should have increased by ~0.2 eV relative to pure CdS, consistent with the composition measured and the elimination of the absorption edge in the short wavelength portion of the QE response. The overall lower QE response shows that even at short circuit, current collection is reduced in this device.

SCAPS simulations of the device performance for SBR64(MAX) indicate that the low short circuit photocurrent, voltage-dependent collection, and increased series resistance are consistent with an excessive positive (spike-type) band offset that apparently results from the increased energy gap in the high-oxygen intermixed (Cd,Zn)(O,S) composition of the buffer layer in this device.

3.3 Process of record sample

Figure 6 displays the STEM-EDS maps taken from the process of record sample, SBR64(POR). There is a strong Cd signal measurable at least 26 nm into the CIGS grains in Figure 6a (compare, for example, with Figures 2a and 4a). The composition of the region in the rectangle in Figure 6a was determined to be Cu 20.2±1.9%, Cd 5.7±0.9%, In 12.0±1.6%, Ga 8.2±0.9%, Se 41.8±3.8%, and O 12.1±1.6%. As with the SBR64(MAX) sample, the Cd signal in the CIGS is accompanied by high oxygen levels, possibly consistent with the Cd incorporation in the CIGS being accompanied by O. From the composition line profile (see Figure S3), we do not observe an apparent decrease of Ga or In concentration as the Cd concentration gradually increases toward the interface. Presumably Cd occupied Cu vacancies in this sample and should lead to *n*-type doping there, as in the case of SBR64(MAX) and SBR64(ZERO). Note that the Cd concentration in the CIGS is higher and Cd is distributed much further (at least 26 nm) into the CIGS than in SBR64(MAX) and SBR64(ZERO), implying that carrier collection may be enhanced at critical depths in these SBR64(POR) samples. The relatively strong response of all devices studied here in the red portion of the

spectrum, based on the QE results, suggests strong carrier collection relatively far into the device. The high concentration of Cd in the CIGS may also lead to a stable Cd-containing secondary phase as suggested in Ref. [36], although no evidence was found for such a phase in the TEM images or diffraction data. For sample SBR64(POR), Zn and O are found in the outer part of the CdS, which is beneficial for harvesting of short wavelength light in the CIGS absorber and may improve the front contact. Analysis of the QE data for this device suggests that the energy gap of the CdS was increased by ~0.1 eV relative to pure CdS. The mixing is not as extreme as in sample SBR64(MAX), where Zn and O are found throughout the CdS but significantly greater than in SBR64(ZERO) where essentially no Zn or O are found in the CdS. The result is only moderate light absorption in the CdS, significantly lower than where no O or Zn is present in the layer, while retaining good junction properties. SCAPS simulations of this device show that modest decrease of electron affinity and increase in energy gap can explain the high device performance, with the positive band offset in the conduction band not enough to inhibit electron transport or add resistance to the device due to the relatively high *n*-type doping of the CdS.

A typical HRTEM image (processed as in Figure 3) of a wurtzite region of CdS epitaxially grown on a CIGS grain from sample SBR64(POR) is shown in Figure 7. The hetero-interface is very coherent and no obvious lattice defects can be seen. The lattice match in this sample is very close based on the lattice fringe spacings. The high crystallinity and epitaxy of the CdS buffer on the CIGS surface indicates that collection of photo-generated carriers in the buffer may be possible and may provide more flexibility in buffer layer engineering. The reduced interface defect density is expected to reduce interface recombination, and the improved crystallinity presumably facilitates electron transport through the buffer, all leading to improved device performance, as evidenced in Table I.

The improved epitaxy relative to the no-oxygen case may be due to the modification of the lattice constant, as shown in Figure 8, which plots the expected lattice constant as a function of

Zn and O composition for the zincblende and wurtzite phases of (Cd,Zn)(O,S), assuming Vegard's Law holds over the entire composition space. Figure 8 shows the a_0 lattice constant that defines the epitaxial relationships we observed in Ref. [14]. We find that for typical low Ga-content CIGS devices (30% Ga), some O and/or Zn content in the buffer is necessary to improve the lattice-match, enhance epitaxy, and form a very high quality interface. Figure 8 also suggests that higher O and/or Zn content in the CdS-derived buffer would improve the likelihood of forming a more coherent interface with graded CIGS devices that incorporate a higher percentage of Ga closer to the absorber-buffer interface. We also see, as discussed above, that a greater excess of O and/or Zn (*e.g.*, >20% O in CdS for typical CIGS compositions) results in nanocrystalline or amorphous growth, leading to poorer carrier transport across the heterojunction.

4. Conclusions

We observe that elemental intermixing of PVD-CdS/CIGS heterojunctions and the epitaxial quality of the CdS buffer layer on CIGS can be tuned by varying the oxygen concentration employed in the PVD process gas during CdS deposition. Relatively high O content inhibits Cu and facilitates Zn migration into the CdS, resulting in a quaternary (Cd,Zn)(S,O) buffer layer. Meanwhile, low to moderate O content enhances crystallinity and epitaxy of the CdS by improving the lattice match with the underlying CIGS. SCAPS simulations suggest that the differences in device parameters between the samples could be explained by changes in band alignment due both to the observed changes in the CdS band gap and a change in the dipole moment at the CdS/CIGS interface. In addition, Cu depletion from the CIGS near-interface region and counter-doping with Cd from the CdS buffer is also controllable with O addition to the process gas. The optimal (moderate) O content in the gas yields the largest penetration of Cd into the CIGS (at least 26 nm), apparently resulting in benefits to the buried p-n homojunction and device efficiency. Our results indicate that high

crystallinity and epitaxy of PVD-CdS on CIGS and the formation of a relatively deep buried p-n homojunction in the CIGS could explain why the PVD-CdS/CIGS solar cell devices studied here can perform as well as devices fabricated with CBD-CdS.

Supporting Information
Supporting Information is available from the Wiley Online Library or from the author.

Acknowledgements
This research was supported by the DOE/EERE SunShot BRIDGE program. A portion of this work was performed under the auspices of the U.S. Department of Energy by Lawrence Livermore National Laboratory under Contract DE-AC52-07NA27344. Work at the Molecular Foundry was supported by the Office of Science, Office of Basic Energy Sciences, of the U.S. Department of Energy under Contract No. DE-AC02-05CH11231. Part of work was carried out at the Center for Microanalysis of Materials at the University of Illinois at Urbana-Champaign, which is partially supported by the U.S. Department of Energy.

References:

[1] I. Repins, M.A. Contreras, B. Egaas, C. DeHart, J. Scharf, C.L. Perkins, B. To, R. Noufi, 19.9%-efficient ZnO/CdS/CuInGaSe2 solar cell with 81.2% fill factor, Progress in Photovoltaics, 16 (2008) 235-239.

[2] A. Romeo, A. Terheggen, D. Abou-Ras, D.L. Batzner, F.J. Haug, M. Kalin, D. Rudmann, A.N. Tiwari, Development of thin-film Cu(In,Ga)Se-2 and CdTe solar cells, Progress in Photovoltaics, 12 (2004) 93-111.

[3] P. Jackson, D. Hariskos, E. Lotter, S. Paetel, R. Wuerz, R. Menner, W. Wischmann, M. Powalla, New world record efficiency for Cu(In,Ga)Se-2 thin-film solar cells beyond 20%, Progress in Photovoltaics, 19 (2011) 894-897.

[4] M.A. Green, K. Emery, Y. Hishikawa, W. Warta, E.D. Dunlop, Solar cell efficiency tables (version 43), Progress in Photovoltaics, 22 (2014) 1-9.

[5] A. Rockett, R.W. Birkmire, CuInSe2 for photovoltaic applications, J Appl Phys, 70 (1991) R81-R97.

[6] D. Hariskos, B. Fuchs, R. Menner, N. Naghavi, C. Hubert, D. Lincot, M. Powalla, The Zn(S,O,OH)/ZnMgO Buffer in Thin-Film Cu(In,Ga)(Se,S)(2)-Based Solar Cells Part II: Magnetron Sputtering of the ZnMgO Buffer Layer for In-Line Co-Evaporated Cu(In,Ga)Se-2 Solar Cells, Progress in Photovoltaics, 17 (2009) 479-488.

[7] N. Barreau, J.C. Bernede, S. Marsillac, C. Amory, W.N. Shafarman, New Cd-free buffer layer deposited by PVD: In2S3 containing Na compounds, Thin Solid Films, 431 (2003) 326-329.

[8] T. Nakada, M. Mizutani, Y. Hagiwara, A. Kunioka, High-efficiency Cu(In,Ga)Se-2 thin-film solar cells with a CBD-ZnS buffer layer, Solar Energy Materials and Solar Cells, 67 (2001) 255-260.

[9] N. Naghavi, D. Abou-Ras, N. Allsop, N. Barreau, S. Buecheler, A. Ennaoui, C.H. Fischer, C. Guillen, D. Hariskos, J. Herrero, R. Klenk, K. Kushiya, D. Lincot, R. Menner, T. Nakada, C. Platzer-Bjorkman, S. Spiering, A.N. Tiwari, T. Torndahl, Buffer layers and transparent conducting oxides for chalcopyrite Cu(In,Ga)(S,Se)(2) based thin film photovoltaics: present status and current developments, Progress in Photovoltaics, 18 (2010) 411-433.

[10] A. Romeo , D. Abou-Ras , R. Gysel , S. Buzzi , D. L. Bätzner , D. Rudmann , H. Zogg , A.N. Tiwari, Properties of CIGS solar cells developed with evaporated II-VI buffer layers, Technical Digest of the 14th International Photovoltaic Science and Engineering Conference, Bangkok, Thailand, (2004) 2.

[11] D. Abou-Ras, G. Kostorz, A. Romeo, D. Rudmann, A. Tiwari, Structural and chemical investigations of CBD- and PVD-CdS buffer layers and interfaces in Cu(In,Ga)Se-2-based thin film solar cells, Thin Solid Films, 480 (2005) 118-123.

[12] M. Rusu, T. Glatzel, A. Neisser, C.A. Kaufmann, S. Sadewasser, M.C. Lux-Steiner, Formation of the physical vapor deposited CdS/Cu(In,Ga)Se-2 interface in highly efficient thin film solar cells, Appl Phys Lett, 88 (2006).

[13] Fraunhofer ISE measurement report to MiaSolé dated Nov. 17 2015.

[14] X.Q. He, G. Brown, K. Demirkan, N. Mackie, V. Lordi, A. Rockett, Microstructural and chemical investigation of PVD-CdS/PVD-CuIn1-xGaxSe2 heterojunctions: a transmission electron microscopy study, IEEE J. Photovolt., 4 (2014) 1625-1629.

[15] X. He, J. Varley, P. Ercius, T. Erikson, J. Bailey, G. Zapalac, D. Poplavskyy, N. Mackie, A. Bayman, V. Lordi, Intermixing and Formation of Cu-Rich Secondary Phases at Sputtered CdS/CuInGaSe 2 Heterojunctions, IEEE J. Photovolt., 6 (2016) 1308-1315.

[16] X. He, T. Paulauskas, P. Ercius, J. Varley, J. Bailey, G. Zapalac, D. Poplavskyy, N. Mackie, A. Bayman, D. Spaulding, R. Klie, V. Lordi, A. Rockett, Cd doping at PVD-CdS/CuInGaSe2 heterojunctions, Solar Energy Materials and Solar Cells, 164 (2017) 128-134.

[17] J.M. Kephart, R.M. Geisthardt, W.S. Sampath, Optimization of CdTe thin-film solar cell efficiency using a sputtered, oxygenated CdS window layer, Progress in Photovoltaics, 23 (2015) 1484-1492.

[18] D.M. Meysing, C.A. Wolden, M.M. Griffith, H. Mahabaduge, J. Pankow, M.O. Reese, J.M. Burst, W.L. Rance, T.M. Barnes, Properties of reactively sputtered oxygenated cadmium sulfide (CdS:O) and their impact on CdTe solar cell performance, J. Vac. Sci. Technol. A, 33 (2015).

[19] B.E. McCandless, H. Hichri, G. Hanket, R.W. Birkmire, Ieee, Vapor phase treatment of CdTe/CdS thin films with CdCl2:O-2, 1996.

[20] E. Regalado-Perez, M.G. Reyes-Banda, X. Mathew, Influence of oxygen concentration in the CdCl2 treatment process on the photovoltaic properties of CdTe/CdS solar cells, Thin Solid Films, 582 (2015) 134-138.

[21] D.R.G. Mitchell, B. Schaffer, Scripting-customised microscopy tools for Digital Micrograph(TM), Ultramicroscopy, 103 (2005) 319-332.

[22] G.M. Liu, T. Schulmeyer, J. Brotz, A. Klein, W. Jaegermann, Interface properties and band alignment of Cu2S/CdS thin film solar cells, Thin Solid Films, 431 (2003) 477-482.

[23] W.D. Gill, R.H. Bube, Photovaltaic properties of CdS/Cu_2S heterojunctions, J Appl Phys, 41 (1970) 3731-3738.

[24] K.W. Boer, The CdS/Cu_2S solar-cell, J Cryst Growth, 59 (1982) 111-120.

[25] D.X. Liao, A. Rockett, Cu depletion at the CuInSe2 surface, Appl Phys Lett, 82 (2003) 2829-2831.

[26] D.X. Liao, A. Rockett, Cd doping at the CuInSe2/CdS heterojunction, J Appl Phys, 93 (2003) 9380-9382.

[27] T. Nakada, A. Kunioka, Direct evidence of Cd diffusion into Cu(In,Ga)Se-2 thin films during chemical-bath deposition process of CdS films, Appl Phys Lett, 74 (1999) 2444-2446.

[28] K. Ramanathan, R. Noufi, J. Granata, J. Webb, J. Keane, Prospects for in situ junction formation in CuInSe2 based solar cells, Solar Energy Materials and Solar Cells, 55 (1998) 15-22.

[29] M. Burgelman, P. Nollet, S. Degrave, Modelling polycrystalline semiconductor solar cells, Thin Solid Films, 361 (2000) 527-532.

[30] J.B. Varley, V. Lordi, Electrical properties of point defects in CdS and ZnS, Appl Phys Lett, 103 (2013).

[31] J.B. Varley, V. Lordi, Intermixing at the absorber-buffer layer interface in thin-film solar cells: The electronic effects of point defects in Cu(In,Ga)(Se,S)(2) and Cu2ZnSn(Se,S)(4) devices, J Appl Phys, 116 (2014).

[32] B. Sadtler, D.O. Demchenko, H. Zheng, S.M. Hughes, M.G. Merkle, U. Dahmen, L.-W. Wang, A.P. Alivisatos, Selective Facet Reactivity during Cation Exchange in Cadmium Sulfide Nanorods, J Am Chem Soc, 131 (2009) 5285-5293.

[33] L.P. Marushko, Y.E. Romanyuk, L.V. Piskach, O.V. Parasyuk, I.D. Olekseyuk, S.V. Volkov, V.I. Pekhnyo, The CuInSe2-CuGaSe2-2CdSe system and crystal growth of the gamma-solid solutions, Journal of Alloys and Compounds, 505 (2010) 101-107.

[34] X. Wu, R.G. Dhere, Y. Yan, M.J. Romero, Y. Zhang, J. Zhou, C. DeHart, A. Duda, C. Perkins, B. To, Ieee, High-efficiency polycrystalline CdTe thin-film solar cells with an oxygenated amorphous CdS (a-CdS : O) window layer, Ieee, New York, 2002.

[35] S.B. Zhang, S.H. Wei, Reconstruction and energetics of the polar (112) and (112)over-bar versus the nonpolar (220) surfaces of CuInSe2, Phys Rev B, 65 (2002).

[36] A. Aquino, A. Rockett, Chemical reactions at CdS heterojunctions with CuInSe2, J. Vac. Sci. Technol. A, 31 (2013).

Table I Device parameters measured from four different CdS/CIGS solar cells with different O concentrations in the CdS process.

Sample	Efficiency (%)	Jsc (mA/cm^2)	FF	Voc (mV)	Dark J_0 (mA/cm^2)	Dark a
SBR64(MAX)(highest O_2)	9.04	30.37	0.49	610	$8x10^{-5}$	2.00
SBR64(POR)(Process of record --moderate O_2)	15.86	31.81	0.74	670	$1x10^{-5}$	1.75
SBR64(LOW)(low O_2)	13.39	31.08	0.73	580	NA	NA
SBR64(ZERO)(No O_2)	11.49	30.08	0.70	540	$1.5x10^{-4}$	1.75

Note that SBR64(MAX) exhibits strong bias-dependent collection resulting in a non-diode like behavior (effective J_0=0.09 mA/cm^2 and a=4) while SBR64(POR) and SBR64(ZERO) show only small increases in J_0 and no change in other parameters.

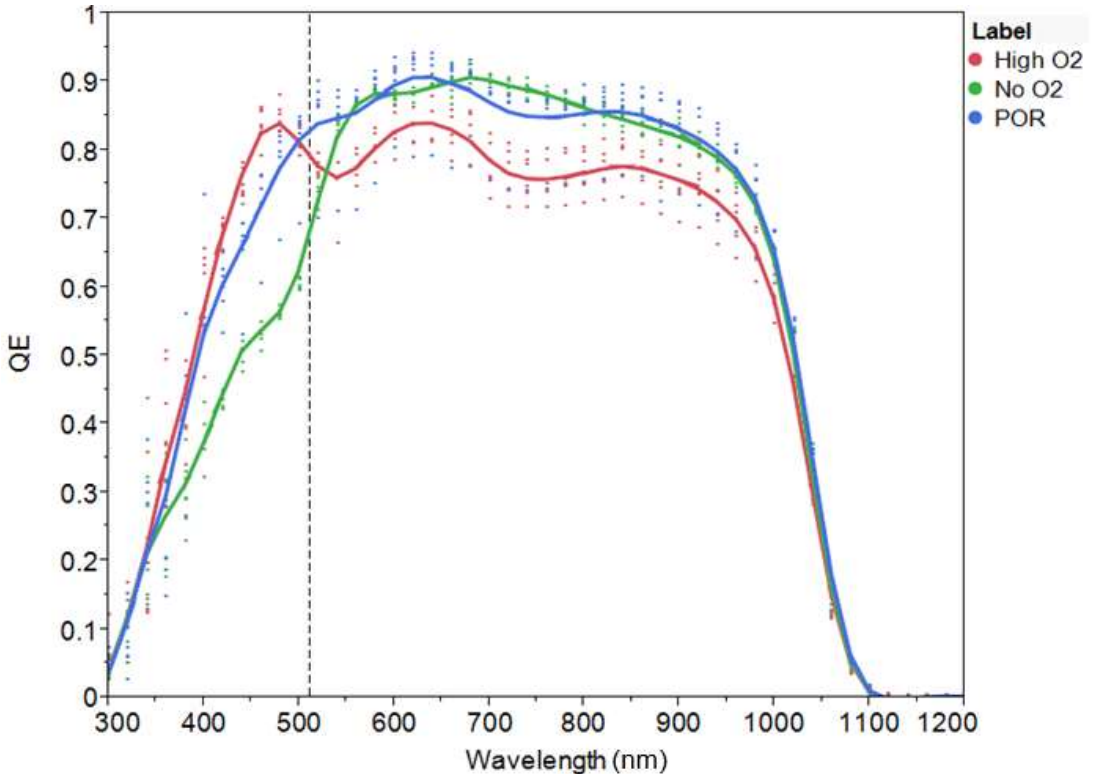

Figure 1. Quantum efficiency data on devices processed under similar conditions to those described for samples SBR64(ZERO), SBR64(MAX), and SBR64(POR).

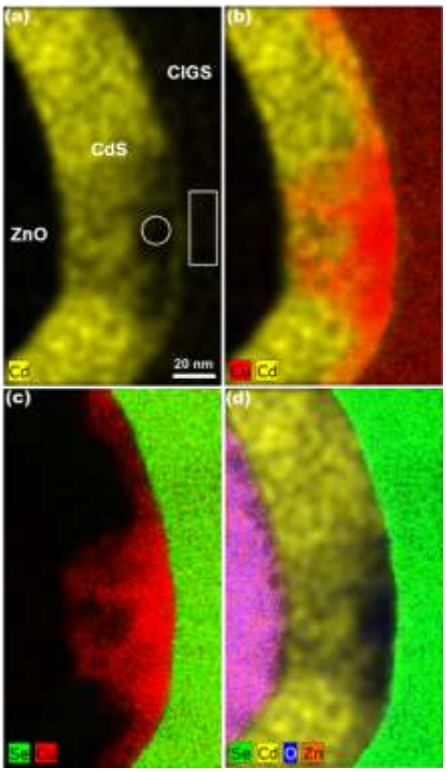

Figure 2. STEM-EDS maps of CdS/CIGS heterojunction in SBR64(ZERO) (no O doping in CdS). (a) Highly Cd depleted region is highlighted by a white circle. EDS quantification from the region denoted by white rectangle suggests Cu deficient CIGS surface doped by Cd. (b) and (c) Note that Cu has nearly penetrated through the whole CdS layer. (d) No pronounced Zn and O doping in CdS.

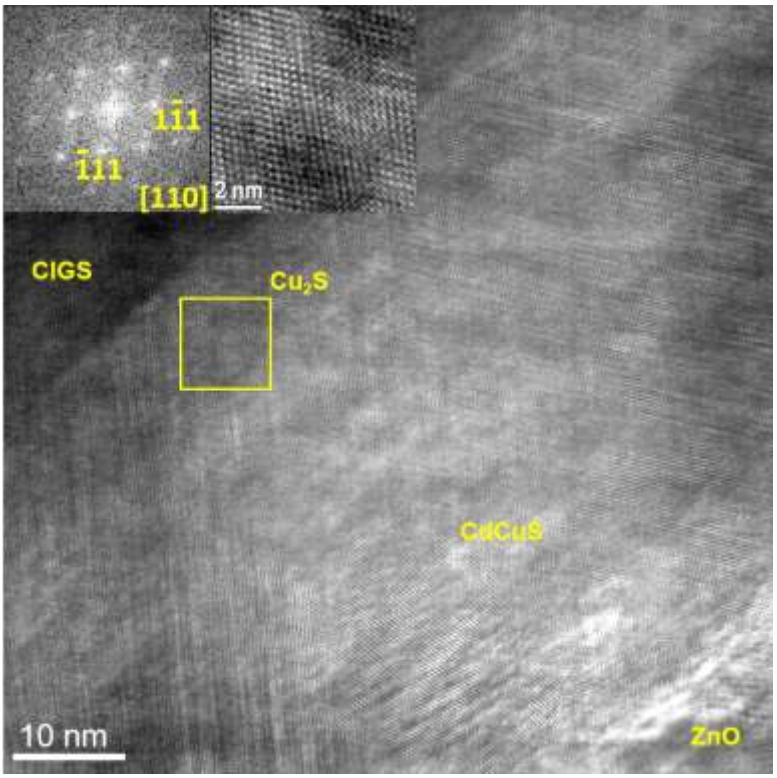

Figure 3. Filtered HRTEM image taken from the highly Cd depleted and Cu doped region in SBR64(ZERO). The hetero-interface is rather coherent. Top left inset shows the FFT pattern from the area indicated by the yellow square (corresponding to the white circle in Figure 2a), which can be well indexed to be cubic Cu_2S [110] zone axis. The high-resolution TEM image shown in inset is the enlarged version of the yellowed square region, suggesting the single-crystalline Cu_2S. © [2016] IEEE. Reprinted with permission from [15].

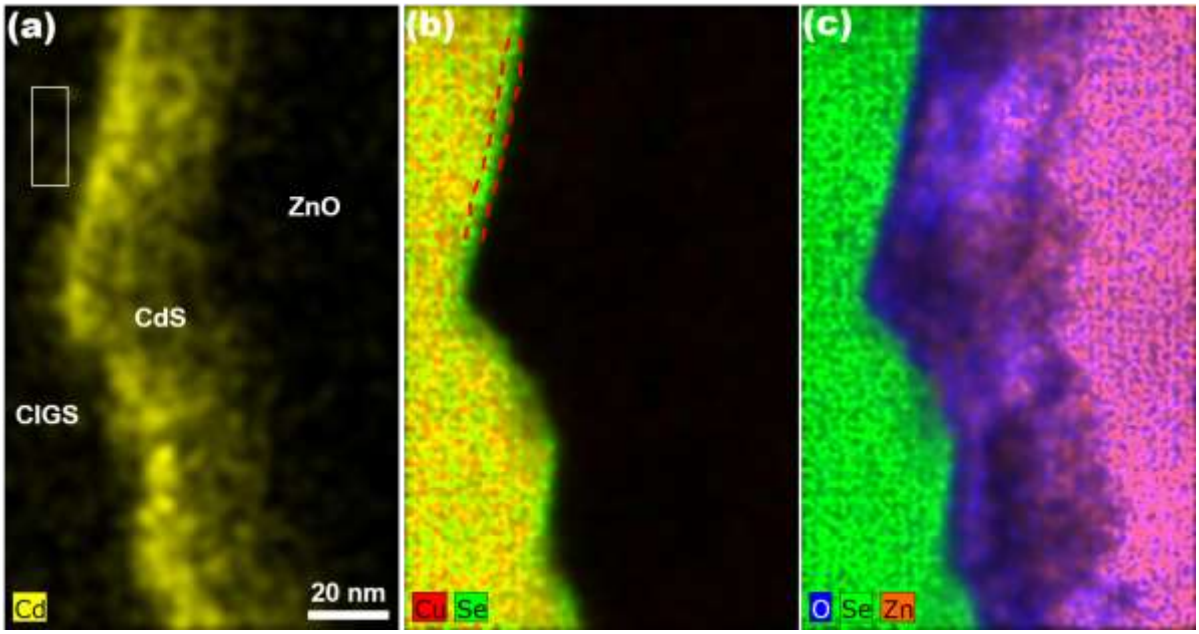

Figure 4. STEM-EDS maps of CdS/CIGS heterojunction in SBR64(MAX) (highest O doping in CdS). (a) No Cu presence in CdS is found. EDS quantification from the region marked by the while rectangle suggests Cd doped $Cu(In,Ga)(Se,O)_2$ phase. (b) The red dotted lines mark Cu deficient layer. From (a) Cd is found in this layer, indicating Cd substituting Cu. (c) Zn is found in the entire CdS layer.

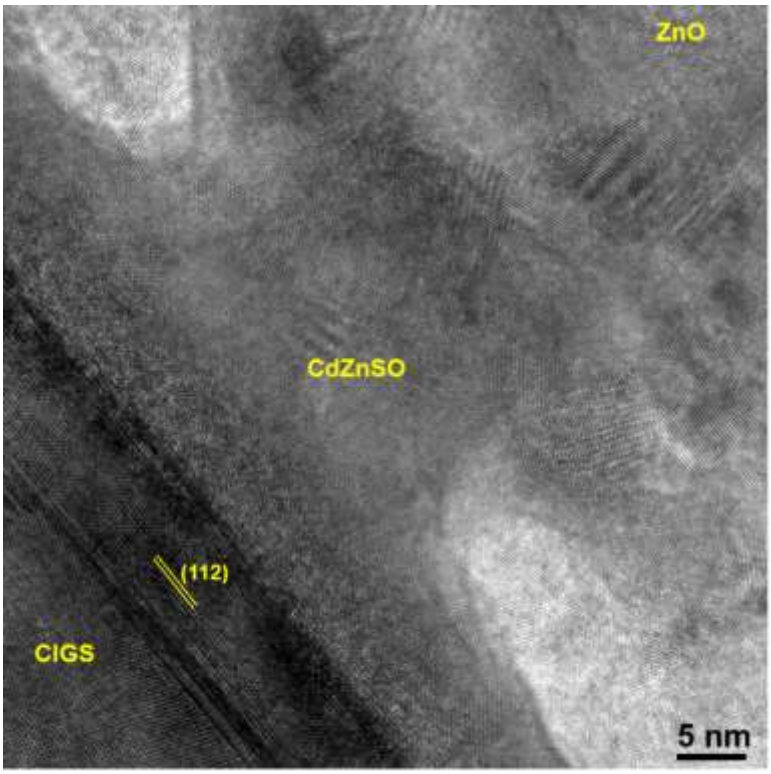

Figure 5. A typical HRTEM image taken from where STEM-EDS maps in Figure 4 are recorded, showing nanocrystallinity of the quaternary compound (Cd,Zn)(S,O). Clearly, very high concentration oxygen doping in CdS degrades the epitaxy and crystallinity of the buffer layer.

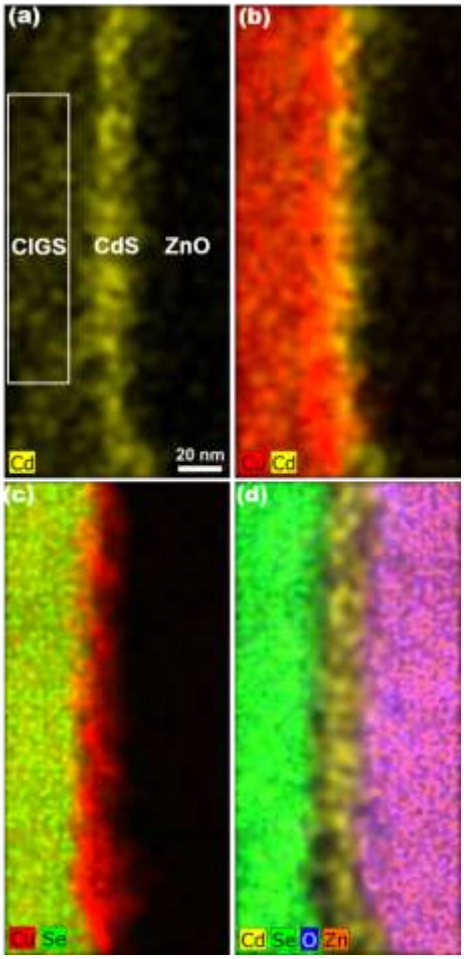

Figure 6. STEM-EDS maps of CdS/CIGS heterojunction in SBR64(POR) (standard sample, modest O doping in CdS). (a) Note the presence of Cd in CIGS. EDS quantification from the region denoted by the white rectangle suggests about 5.7 at% Cd. (b) and (c) Significant Cu penetration into CdS is observed. (d) Zn is found in the outer potion of the CdS layer.

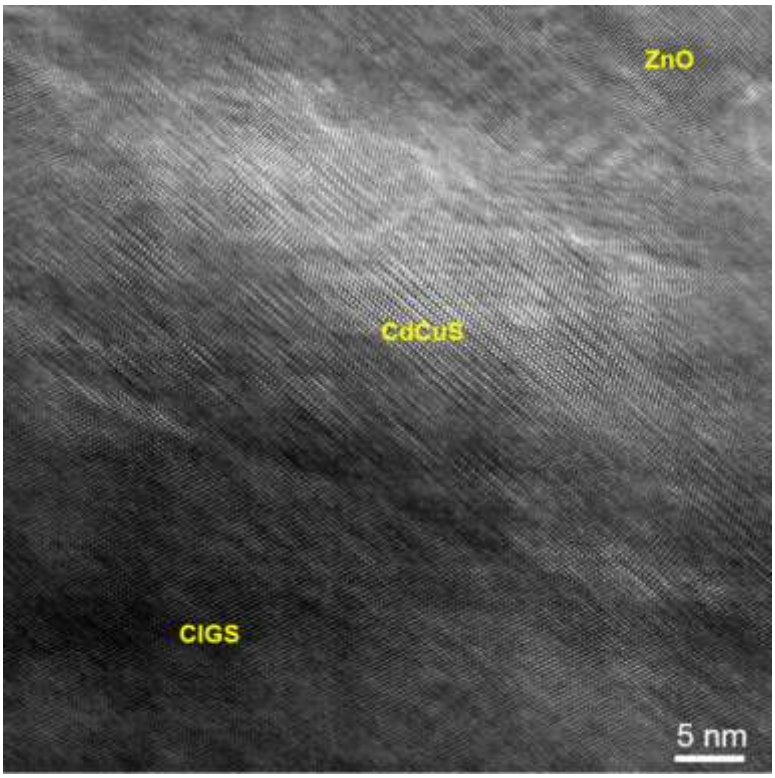

Figure 7. Filtered HRTEM image taken from the region where Figure 6 is acquired. Hexagonal $Cd_xCu_{1-x}S$ phase with high crystallinity is observed epitaxially on CIGS. The epitaxial relationship can be found in Ref. [14].

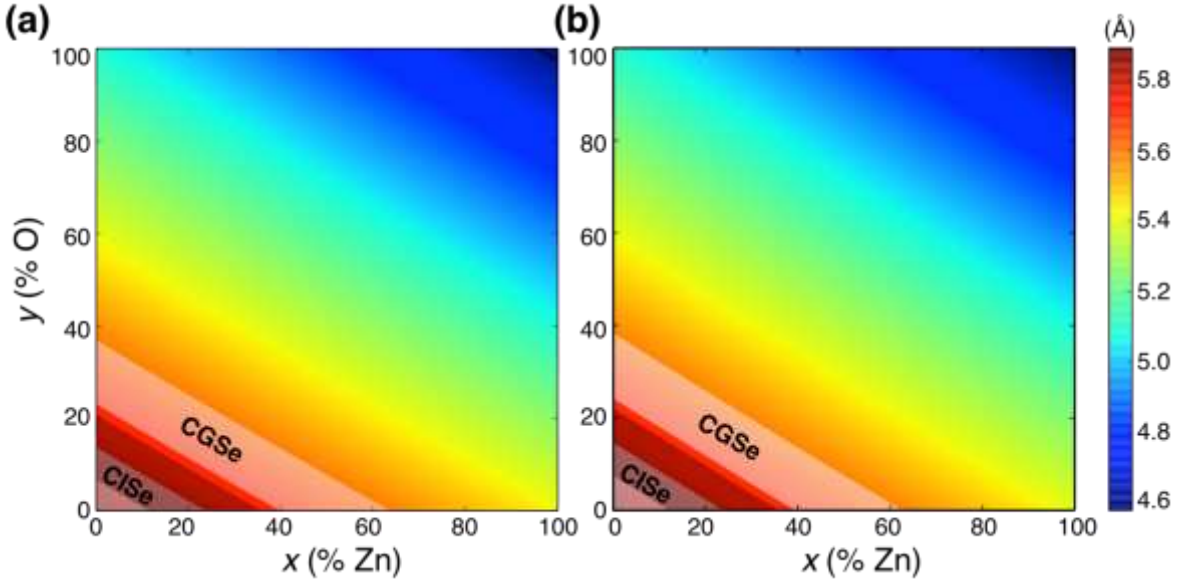

Figure 8. Plot of the expected buffer lattice constant, a_0, as a function of composition for the zincblende (a) and wurtzite (b) phases assuming Vegard's Law holds for the pure compounds (CdS, CdO, ZnS, and ZnO). The shaded regions indicate the compositions necessary to obtain lattice-matching within 1% to pure $CuInSe_2$ and $CuGaSe_2$ (white shading) and typical 30% Ga-content CIGS (dark shading) following the epitaxial relationships found in Ref. [14]. The plots reveal that some O content helps facilitate epitaxy on the absorber as observed in samples like SBR64(POR).

The oxygen content in the sputtering gas during the PVD deposition of CdS buffer layer can be used as a means to effectively control elemental intermixing between CdS and $Cu(InGa)Se_2$ and the crystallinity of CdS in CIGS PV devices. More O suppresses Cu from CIGS and promotes Zn from ZnO into CdS and induces nanocrystalline CdS, while Cu_2S phase was formed and epitaxially grown on $Cu(InGa)Se_2$ when O was involved.

Keyword Solar cells

Xiaoqing He, Peter Ercius, Joel Varley, Jeff Bailey, Geordie Zapalac, Tim Nagle, Dmitry Poplavskyy, Neil Mackie, Atiye Bayman, Vincenzo Lordi*, Angus Rockett*

The role of oxygen doping on elemental intermixing at the PVD-CdS/$Cu(InGa)Se_2$ heterojunction

ToC figure

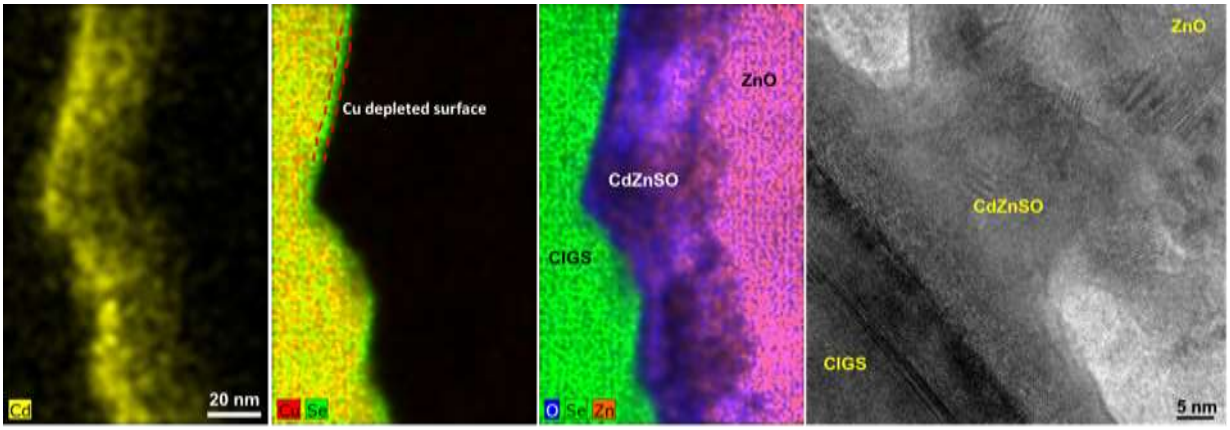

Supporting Information

The role of oxygen doping on elemental intermixing at the PVD-CdS/Cu(InGa)Se_2 heterojunction

Xiaoqing He, Peter Ercius, Joel Varley, Jeff Bailey, Geordie Zapalac, Tim Nagle, Dmitry Poplavskyy, Neil Mackie, Atiye Bayman, Vincenzo Lordi, Angus Rockett**

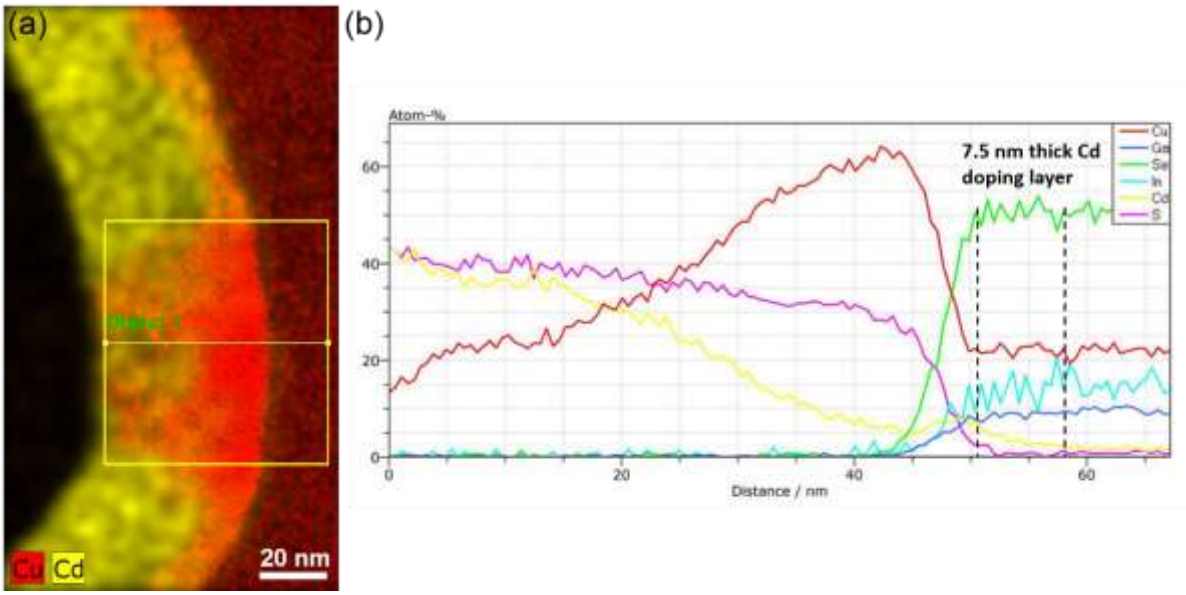

Figure S1. (a) STEM-EDS maps of SBR64(ZERO) showing the Cu rich domain is distributed through the CdS layer. (b) Compositional line profiles integrated from the yellow rectangular box in (a) showing about 7.5 nm thick Cd doped CIGS layer as indicated by two vertical dashed lines.

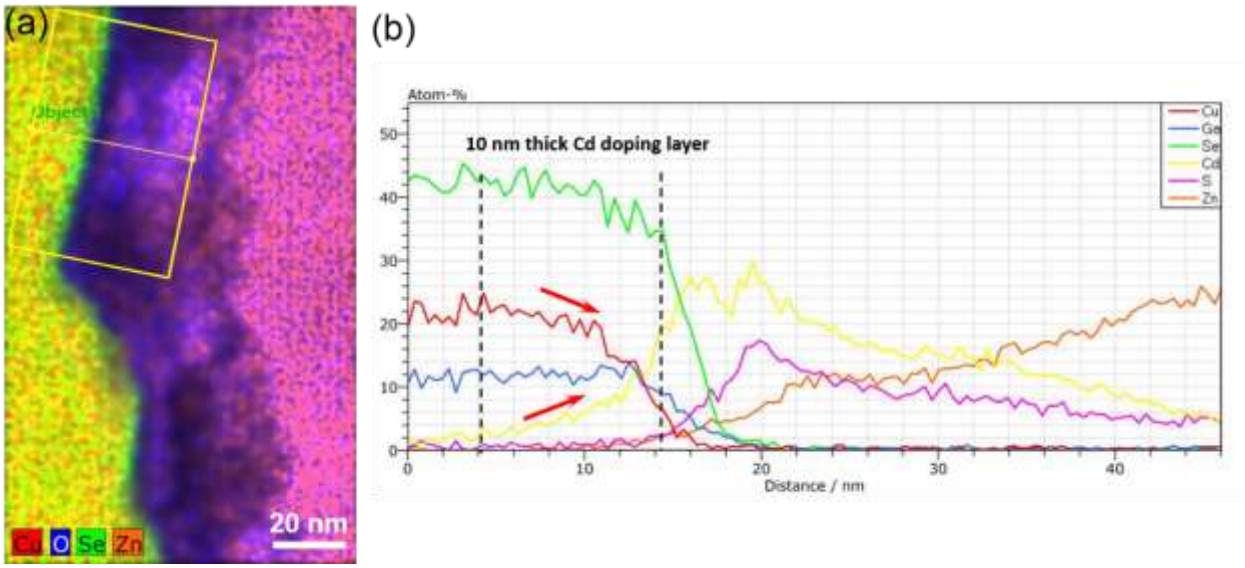

Figure S2. (a) STEM-EDS maps of SBR64(MAX) showing Zn and O are present through the whole CdS layer. (b) Compositional line profiles integrated from the yellow rectangular box in (a) showing about 10 nm thick Cd doped CIGS layer as indicated by two vertical dashed lines. The line profiles of O and In are not shown for better clarity of Cu and Cd. The two red arrows highlight Cd concentration increasing toward the interface with Cu decreasing, indicating Cd substituting Cu.

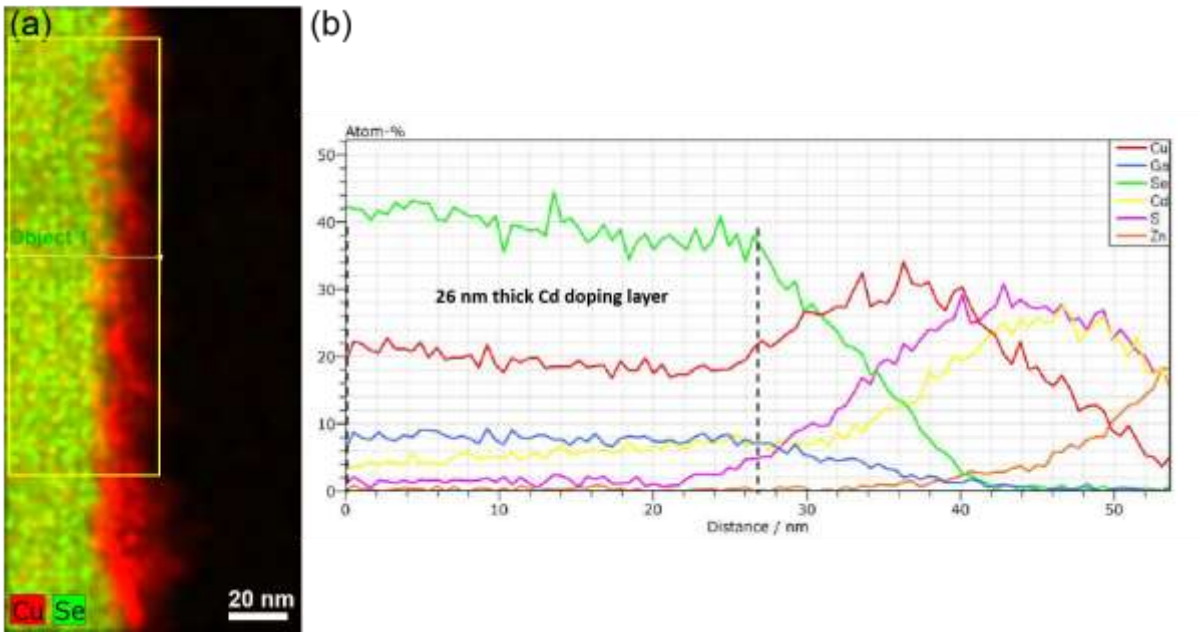

Figure S3. (a) STEM-EDS maps of SBR64(POR) showing Cu is present nearly through the whole CdS layer. (b) Compositional line profiles integrated from the yellow rectangular box in (a) showing at least 26 nm thick Cd doped CIGS layer as indicated by two vertical dashed lines. The line profiles of O and In are not shown for better clarity of Cu and Cd. Zn is seen in the outer part of CdS layer.